
# ONET: Operator network for randomized and robust battery health estimation using operation condition and cycling data matching

Journal of Power Sources 672 (2026) 239592

Contents lists available at ScienceDirect

Journal of Power Sources

journal homepage: www.elsevier.com/locate/jpowsour

# ONET: Operator network for randomized and robust battery health estimation using operation condition and cycling data matching

Hang Hu [a], Chen Liang [b,c], Xinghao Huang [b], Huadong Mo [c,*], Changfu Zou [d,**], Shengyu Tao [b,d,***]

[a] Department of Mechanical Engineering, Tsinghua University, Beijing, 100084, China
[b] Institute of Data and Information, Tsinghua University, Shenzhen, 518055, Guangdong, China
[c] School of Systems and Computing, The University of New South Wales, Canberra, ACT, 2610, Australia
[d] Department of Electrical Engineering, Chalmers University of Technology, Gothenburg, 41296, Sweden

## HIGHLIGHTS

- ONET-based framework mapping degradations to the operational conditions.
- Achieving end-to-end SOH estimation using only short 0.2V charging segments.
- Integrating attention mechanism for robust performance across diverse conditions.
- Compact model (<230 KB) enabling efficient edge deployment in battery management systems.
- Evaluated on 121 cells with two chemistries under varied operating conditions.

## ARTICLE INFO

*Keywords:*
Batteries
Health estimation
Operator learning
Charging segment
Operation condition

## ABSTRACT

Robust state-of-health (SOH) estimation is critical for ensuring the reliability and safety of lithium-ion batteries. However, robust estimation across diverse operating conditions often necessitates computationally intensive strategies, such as transfer learning and associated data acquisition cost and time, challenging their practical deployment. This study presents an operator learning neural network (ONET) enabled SOH estimation, which leverages the conditional dependencies between operation conditions and resulted battery operating data to help explicit utilization of operation conditions as an additional information source for state estimation, which is currently underinvestigated. The ONET consists of a trunk network captures the underlying degradation patterns from partial charging segments, while a branch network model the impact of operational conditions on these patterns. An attention-based multi-feature fusion (AMFF) was proposed to produce operation-condition dependable SOH estimates, which adaptively combines outputs of the trunk and branch networks by dynamically learning attention weights to assess their relative importance. Validated on a two chemistries dataset (NCA and NCM battery chemistry) under diverse temperatures (25, 35, and 45 $^{\circ}C$) and charging rates (0.25, 0.5, and 1C), the proposed ONET exhibits highly accurate SOH estimation using 0.2 V partial charging segments, achieving performance to state-of-the-art models with a mean absolute error (MAE) of 0.438%, a mean absolute percentage error (MAPE) of 0.496%, and an improved coefficient of determination ($R^2$) of 0.991 across different dataset splits. Practically, ONET is lightweight with a memory size of 230 KB, an 88.7% reduction in memory compared to a reference model, making it suitable for deployment on resource-constrained edge devices. Moreover, AMFF-ONET demonstrates robustness against noise injections, maintaining accuracy ($R^2 > 0.75$) under a low signal-to-noise ratio up to 30 dB. Broadly, proposed ONET demonstrates advantages of learning inherited conditional matching between battery operation conditions and resulted cycling data, providing robust while lightweight solutions to health state monitoring and evaluation of critical energy infrastructures.

* Corresponding author.
** Corresponding author.
*** Corresponding author. Institute of Data and Information, Tsinghua University, Shenzhen, 518055, Guangdong, China.
*E-mail addresses:* huadong.mo@unsw.edu.au (H. Mo), changfu.zou@chalmers.se (C. Zou), Shengyu.tao@chalmers.se (S. Tao).

https://doi.org/10.1016/j.jpowsour.2026.239592
Received 1 December 2025; Received in revised form 4 February 2026; Accepted 7 February 2026
Available online 18 February 2026

## 1. Introduction

The accelerating transition toward carbon neutrality has spurred substantial growth in the energy storage sector over the past ten years. As a pivotal technology, lithium-ion batteries serve a vital function in diverse fields, extending from grid-scale power applications to consumer electronics and electric mobility [1]. Current market analyses forecast that worldwide lithium-ion battery demand will surge to 1156 GWh by 2026 [2]. This dramatic increase underscores the critical need for accurate estimation of battery health parameters, including state of charge (SOC) [3–5], state of health (SOH) [6], and remaining useful life (RUL) [7]. Accurate estimation of these parameters is essential to enhance performance, prevent system failures, and mitigate safety risks associated with capacity degradation. Unlike measurable quantities such as voltage or temperature, SOH cannot be determined by a simple sensor reading during real-time operation. Instead, its accurate measurement requires offline testing or time-consuming laboratory procedures, which are unfeasible in online applications. This constraint underscores the need for data-driven SOH estimation models capable of assessing battery health from operational data across diverse operating conditions, while remaining computationally efficient for online implementation.

Artificial intelligence (AI) has become a prominent method for SOH estimation, standing out among traditional model-driven and data-driven approaches [8–12]. Various AI-driven SOH estimation models have been developed, such as Gaussian Process regression models [13–16], Recurrent Neural Networks (RNNs) [17–20], Transformer models [21], Random Forest models [22,23], and Extreme learning machine models [24,25]. Despite their promise, the practical deployment of existing AI-driven SOH estimation models is severely confounded by several obstacles, including reliance on hand-crafted features, the sensitivity to shifts in operational conditions, and high computational complexity [26]. A primary focus of research in addressing these limitations was the development of end-to-end models that operate on segmented charging data, thus bypassing the need for manual feature engineering. RNNs have gained prominence as a widely adopted approach. Li et al. [27] developed an end-to-end LSTM architecture that processes raw voltage-time sequences extracted from a voltage range of 3.65-3.89 V. In Ref. [28], a bidirectional GRU (BiGRU) network was employed to extract health features from partial discharge profiles, while a Transformer architecture mapped these features to SOH estimates. Besides, Convolutional Neural Networks (CNNs), renowned for their superior feature extraction capabilities, have been widely adopted for automated health feature extraction from partial sequences for SOH estimation [29–31]. adopted convolutional neural networks to establish a direct mapping between partial segments and SOH values. Zhang et al. [32] introduced a model comprising 13 stacked CNN blocks for SOH estimation, utilizing 350 mV partial Q-V sequences. In Ref. [33], a residual CNN model was developed for SOH estimation, which accepts any V-I sequence of length equivalent to 36% of the normal capacity as input. In contrast to previous methods requiring sequences with specified voltage locating, CNN-based models effectively process partial charging sequences starting from any location while preserving estimation reliability. Some advanced network structures were introduced to estimate SOH with partial segments. A deep-learning framework based on BiGRU and structured kernel interpolation Gaussian process regression was proposed in Ref. [34]. The proposed framework utilized 10-min segments of current-voltage-temperature (I-V-T) profiles, randomly sampled from discharge processes, to perform accurate SOH estimation. The proposed ensemble learning framework provides an effective solution for partial sequence utilization, enabling robust SOH estimation. Tian et al. [35] proposed a deep neural network to estimate SOH value with any 0.3 V voltage segment via reconstructing the constant-current charging curve. In Refs. [36,37], multiple base learners were trained and estimated on a specific part of the charging curve, with their outputs concatenated as input features for a meta-learner to generate the final SOH estimate. The aforementioned models leverage partial charge and discharge segment data to achieve SOH estimation with the end-to-end approaches. However, such models still encounter challenges related to poor adaptability in varying battery operation conditions, without explicitly using operation-condition and cycling data dependencies.

This lack of robustness can be largely attributed to the fact that these state-of-the-art models are not explicitly conditioned on operational parameters (such as temperature, charge rate, and battery chemistry), but instead treat them as implicit factors to be inferred from the training data. Consequently, their ability to generalize across operational conditions is impaired. To address the limited adaptability of the aforementioned end-to-end models, transfer learning has emerged as a promising strategy. Transfer learning via fine-tuning is the predominant strategy in the SOH estimation [38–43]. In the fine-tuning strategy, parts of the model pre-trained on the source domain are further adapted using target domain data. For example, Sahoo et al. [44] successfully transferred the artificial neural network (ANN) model to diverse datasets, including CALCE and NASA, by fine-tuning only the second layer of the pre-trained network. However, the position of the input sequence is fixed. Li et al. [45] fine-tuned a CNN SOH estimation model by retraining convolutional and fully-connected layers, enabling the adapted model to generalize effectively across batteries under diverse operating conditions. Yao et al. [46] proposed a multi-domain transfer learning strategy based on a handcrafted feature-based CNN-LSTM model to estimate the SOH under dynamic operating conditions, including varying charge-discharge depths and current rates. Similar to previous approaches, only the higher-level layers were retrained and fine-tuned online using the target domain data. Another widely used transfer learning strategy is the feature-based method, which adapts the representation of source-domain data to improve alignment with the target domain task [47–49]. In Ref. [50], a feature-based transfer strategy using ElasticNet was proposed to align the target and source domains. Besides [48,51], adopted correlation alignment (CORAL) to fix feature divergence across domains. In Ref. [52], Lu et al. trained ANN models by simultaneously minimizing SOH estimation error on the source domain and reducing distribution discrepancy. Although the transfer learning-based method is straightforward and widely applicable, it suffers from limitations, including high labor intensity and frequent dependence on large amounts of target-domain data. Moreover, transfer learning requires considerable expert effort to optimize hyperparameters during the secondary training phase to ensure effectiveness [53].

In this study, we proposed a transfer-free ONET that presents a unified and lightweight approach for rapid and robust SOH estimation across diverse operating conditions. The core principle is to decouple the learning of degradation patterns from the influence of operational conditions. This strong foundation for generalization is further enhanced by an attention-based multi-feature fusion (AMFF) module, which dynamically assesses the relative importance of trunk and branch network outputs. This adaptive weighting elevates the model's accuracy and robustness, achieving a mean absolute error (MAE) of 0.438%, a mean absolute percentage error (MAPE) of 0.496%, and an improved coefficient of determination ($R^2$) of 0.991 in diverse operation conditions. The lightweight framework exhibits a compact end-to-end architecture with a model size under 230 KB, providing significant advantages for resource-constrained edge computing applications. To the best of our knowledge, this work constitutes the first application of a nonlinear operator learning to the problem of battery SOH estimation using the inherited relationship between operation conditions and resulting operation data. It is important to note that the robustness discussed in this study primarily refers to the framework's capability for unified multi-condition modeling within the defined operational envelope of the training data. Unlike zero-shot transfer learning, the proposed ONet architecture focuses on integrating diverse operational parameters and chemistries into a single, cohesive operator mapping. Unlike traditional models that require specific retraining or transfer

learning for different operating environments, the proposed ONET architecture directly learns the conditional mapping between diverse operational parameters and degradation patterns. This allows a single model to provide accurate SOH estimates across the entire operational envelope spanned by the training data, significantly enhancing its practical utility for complex applications where diverse conditions are encountered simultaneously.

The rest of the paper is organized as follows. Section II introduces the dataset used in this paper. Section III describes methodologies. In Section IV, a comprehensive analysis was conducted to evaluate the SOH estimation performance of the AMFF-ONET framework. Finally, Section V provides the conclusion of this study.

## 2. Dataset description

We utilize the Tongji Battery Dataset to simulate real-world lithium-ion battery operating conditions [54]. The dataset includes three types of lithium-ion battery (NCA battery with $LiNi_{0.86}Co_{0.11}Al_{0.03}O_2$ as positive electrode, NCM battery with $LiNi_{0.83}Co_{0.11}Mn_{0.07}O_2$ as the positive electrode, and NCA + NCM battery with the positive electrode composed of $42 \pm 3$ wt.% $Li(NiCoMn)O_2$ blended with $58\pm$ 3 wt.% $Li(NiCoAl)O_2$). This study employs datasets composed of the first two types of batteries (NCA battery and NCM battery), which are noted as Dataset 1 and Dataset 2, as they contain more extensive experimental data. Finally, a total of 121 batteries with two chemistries and multiple operating conditions were used in the work. The operating conditions for the two datasets are listed in Table 1. More detailed experiment information can be found in Ref. [54].

## 3. Methods

This work introduces a novel operator-learning framework designed to overcome the fundamental limitations of current SOH estimation methods. We aim to develop a unified, end-to-end solution that directly leverages partial $\Delta Q - V$ sequences to achieve robust performance across diverse operational conditions. Fig. 1 depicts the overall framework. This section first introduces the data preparation process, followed by a detailed elaboration of the ONET-based SOH estimation framework, illustrating its capability to estimate SOH using partial $\Delta Q-V$ sequences across varying operating conditions.

### 3.1. Data preparation

Previous studies demonstrated that the constant-current charging phase incorporates sufficient information for SOH estimation [17]. Furthermore, constant-current charging data are more readily obtainable in real-world applications, as they constitute the dominant phase in the lithium-ion battery charging process. To ensure practical applicability, our framework requires charging voltage ($V$) and incremental capacity ($\Delta Q$) measurements, which represent the most widely available data in BMS. Therefore, the $Q-V$ sequences extracted from the constant-current charging phase are adopted in the following discussion. The end-to-end nature of the proposed framework simplifies data preparation work to two key steps: outlier elimination and $Q-V$ sequence partitioning via the moving window method. The 3-Sigma Rule was first introduced to remove outliers. Afterwards, linear interpolation was used to resample the $Q-V$ sequence.

**Table 1**
Description of the two datasets.

| Dataset | Temperature (°C) | Charge rate (C) | Discharge rate (C) | Pieces |
|---|---|---|---|---|
| 1 | 25 | 0.25 | 1 | 7 |
| 1 | 25 | 0.5 | 1 | 19 |
| 1 | 25 | 1 | 1 | 9 |
| 1 | 35 | 0.5 | 1 | 3 |
| 1 | 45 | 0.5 | 1 | 28 |
| 2 | 25 | 0.5 | 1 | 23 |
| 2 | 35 | 0.5 | 1 | 4 |
| 2 | 45 | 0.5 | 1 | 28 |

Fig. 2 shows the resampled SOH curves of two datasets. It can be observed that batteries operating under different conditions exhibit significantly distinct degradation patterns, thereby substantially complicating SOH estimation within a unified model.

Finally, a moving window method was adopted to extract partial $\Delta Q-V$ sequences. The window length was set to match the length of the partial sequence, and the window was advanced along the charging voltage axis with a step size of 0.01 V. Unless otherwise specified, the window length is set as 0.2 V by default. The initial and terminal voltages of the moving window were collected and denoted as $V_{start}$ and $V_{end}$, respectively. Ten uniformly distributed capacity data points $Q_1, Q_2, \ldots, Q_{10}$ inside the moving window were computed using the resampling $Q-V$ curve, and the incremental capacity sequence was subsequently computed using Equation (1).

$$\Delta Q_i = Q_i - Q_1. \tag{1}$$

Where $Q_i$ is the $i_{th}$ capacity data point and $Q_1$ is the first data point. Finally, the obtained input data can be denoted as $[\Delta Q, V_{start}, V_{end}, C_{rate}, temp, type]$, $\Delta Q = [\Delta Q_1, \Delta Q_2, \ldots, \Delta Q_{10}]$, $C_{rate}$ is the charging rate, *temp* is the working temperature, and *type* is a categorical label denoting the battery chemistry, where 0 represents NCA and 1 represents NCM. The label SOH can be calculated by the following equation.

$$SOH_i = \frac{Capacity_i}{Capacity_0}. \tag{2}$$

Where subscript $i$ indicates the cycle number and *Capacity* denotes the battery capacity.

### 3.2. SOH estimation framework

ONET is an operator approximator proposed in Ref. [55], which can accurately approximate any nonlinear continuous operator. The mathematical expression of ONET is described by Equation (3). It can be observed that the ONET comprises two distinct networks: (1) a branch network responsible for encoding the input function, and (2) a trunk network that approximates a set of basis functions. In the conventional ONET, the final output is computed by the inner product of these two networks' outputs. The universal approximation theorem for nonlinear operators, as demonstrated in the original work by Ref. [55], establishes that ONET can approximate any continuous nonlinear operator to arbitrary accuracy with sufficiently large branch and trunk networks.

$$G(u)(y) \approx \sum_{k=1}^{p} \underbrace{b_k(u(x_1), u(x_2), \ldots, u(x_m))}_{\text{branch network}} \underbrace{t_k(y)}_{\text{trunk network}}, \tag{3}$$

In our work, we aim to estimate the SOH value under different operation conditions using partial $\Delta Q-V$ sequences. Therefore, the SOH estimation can be modeled as a function $f(\Delta Q)$ conditioning on five operational parameters: $V_{start}, V_{end}, C_{rate}, temp, type$, which can be described as the following equation.

$$SOH = g(f(\Delta Q), V_{start}, V_{end}, C_{rate}, temp, type). \tag{4}$$

Equation (4) can be reformulated as a composition of two functions forming a nonlinear functional operator, where the function $f$ encodes $\Delta Q$ into a latent space, acting as the "capacity degradation basis function", and $g$ combines this latent representation with other conditioning inputs in a nonlinear manner to estimate SOH. To effectively model this nonlinear functional operator, we adopt the ONET framework, where $f$ and $g$ are parameterized as the trunk network and branch network, respectively. The overall architecture of our SOH estimation framework is visually presented in Fig. 3.

In this work, the functions $f$ and $g$ are implemented as two fully

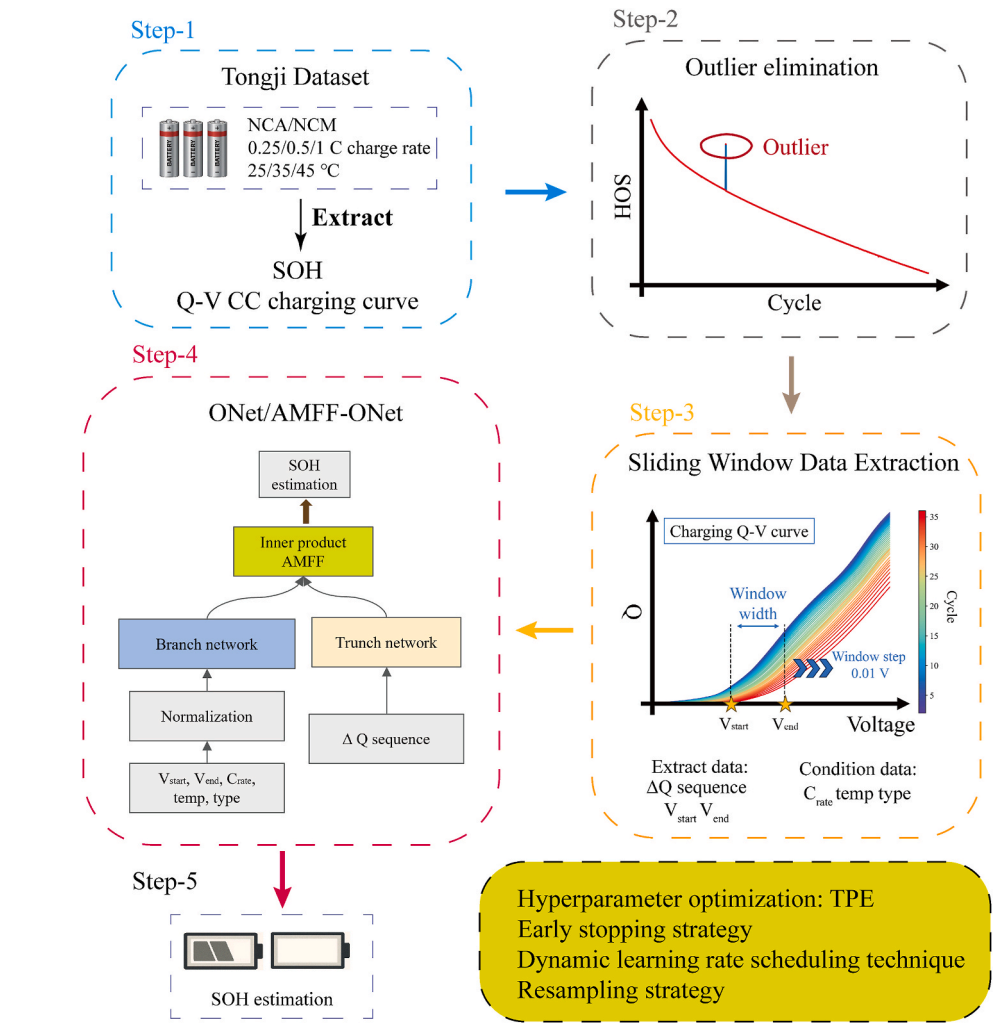


**Fig. 1.** The overall framework for SOH estimation.

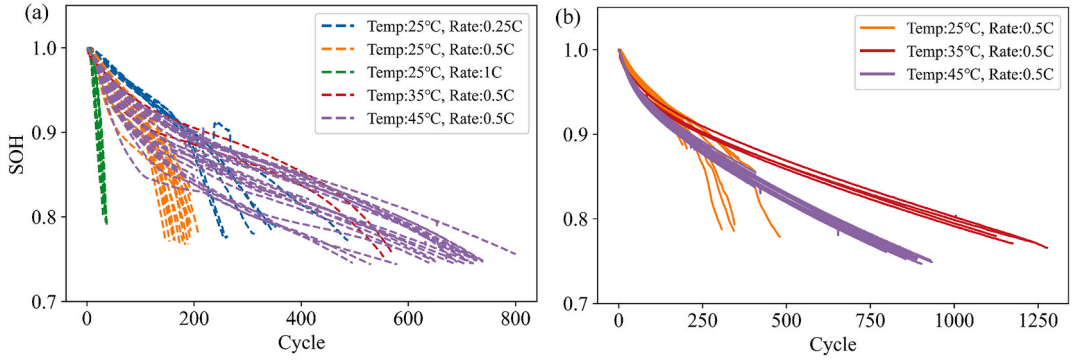


**Fig. 2.** The resampled SOH curves of two datasets. (a) Dataset 1 and (b) Dataset 2.

connected neural networks. The trunk network takes the $\Delta Q$ sequence as input, while the branch network $g$ receives a concatenated input of $V_{start}$, $V_{end}$, $C_{rate}$, $temp$, $type$. In other words, the branch network provides the "environment" information for the trunk network. The final result is calculated by the inner product or the attention mechanism, which will be described in the next sub-section.

To ensure numerical stability, all input data were normalized to the $[0, 1]$ range. $V_{start}$ and $V_{end}$ were normalized by 2.9 and 4.21 V, and $temp$ was normalized by divide with 100. The remaining input data were already within the $[0, 1]$ range, thus requiring no additional normalization.

### 3.3. Fusion network

As stated above, in the paper [55], the final result is generated by the inner product. In this work, the attention mechanism is introduced to enrich fusion capability. Chen et al. [56] proposed a multi-feature fusion framework based on the attention mechanism, abbreviated as AMFF, to elucidate the contributions of each input channel. In our work, the attention module (AMFF) is introduced to dynamically weight and

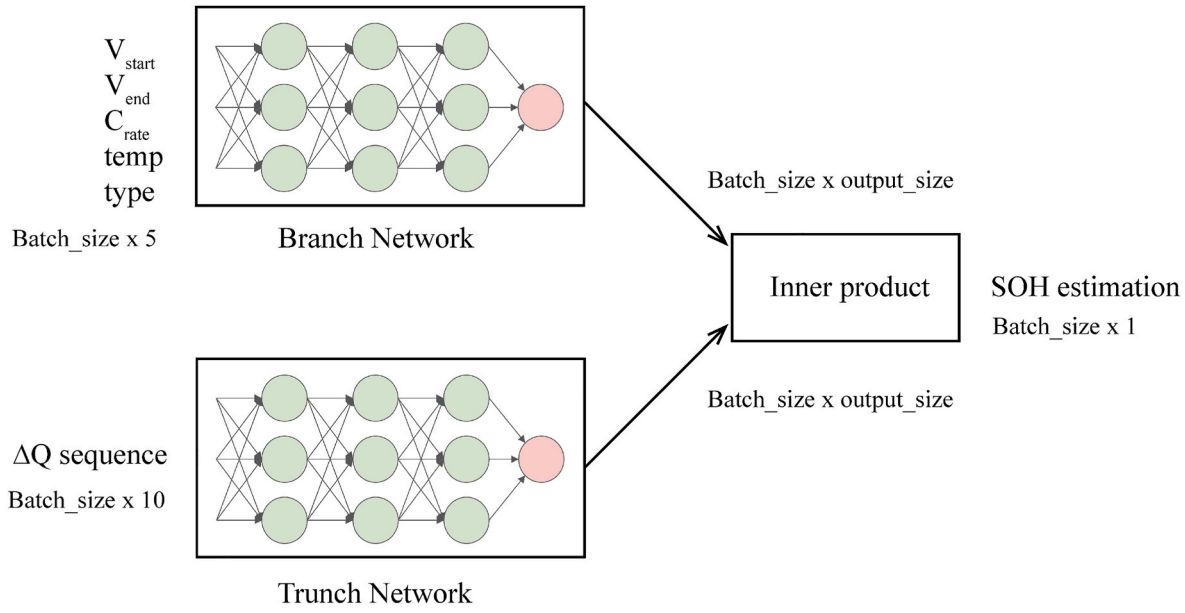


**Fig. 3.** A schematic representation of the ONET-based SOH estimation framework.

aggregate the outputs from the trunk network and branch network, as depicted in Fig. 4.

**Algorithm 1**
ONET Forward Pass Procedure

**Require:** $x_{\Delta Q}$: Input partial incremental capacity sequence, $[\Delta Q_1, \ldots, \Delta Q_{10}]$; $x_{cond}$: Input operating conditions, $[V_{start}, V_{end}, temp, C_{rate}, type]$.
**Ensure:** $SOH_{est}$: The estimated State of Health value.
**procedure** ONET($x_{\Delta Q}, x_{cond}$)
*//Process inputs through branch end trunk networks*
$O_{trunk} \leftarrow TrunkNework(x_{\Delta Q})$ *//Get basis functions output*
$O_{branch} \leftarrow$ Branch$Network(x_{cond})$ *//Get coefficients output*
*//Fuse outputs using Inner Product*
$SOH_{est} \leftarrow \sum_{i=1}^{N} (O_{trunk}[i] \cdot O_{branch}[i])$ *//N is the output size*
**Return** $SOH_{est}$
**end procedure**

The outputs from the trunk and branch networks are initially concatenated, then processed through a linear layer with tanh activation, followed by a Softmax layer that generates two normalized attention weights. The final SOH estimation is derived by transforming the attention-weighted tensor through a multi-layer linear transformation module. The multi-layer linear transformation module consists of four fully-connected (FC) layers employing *ReLU* activation functions with hidden dimensions of *output_size*, *output_size*/2, *output_size*/2, and 1, where *output_size* is the output size of the trunk network or branch network. The pseudocode implementations of the ONET and AMFF-ONET architectures are formally specified in Algorithm 1 and Algorithm 2, respectively.

The AMFF module utilizes a dynamic weighting mechanism through trainable attention scores, effectively capturing the relative importance of features from both the trunk and branch networks and adaptively fusing them. Furthermore, the subsequent multi-layer linear transformation module enhances the model's estimation capability. The inner product operation exhibits superior computation efficiency and enhanced mathematical interpretability, which can be described as a linear combination of basis functions (Trunk network output) modulated by input-dependent coefficients (Branch network output).

**Algorithm 2**
AMFF-ONET Forward Pass Procedure

(*continued on next page*)

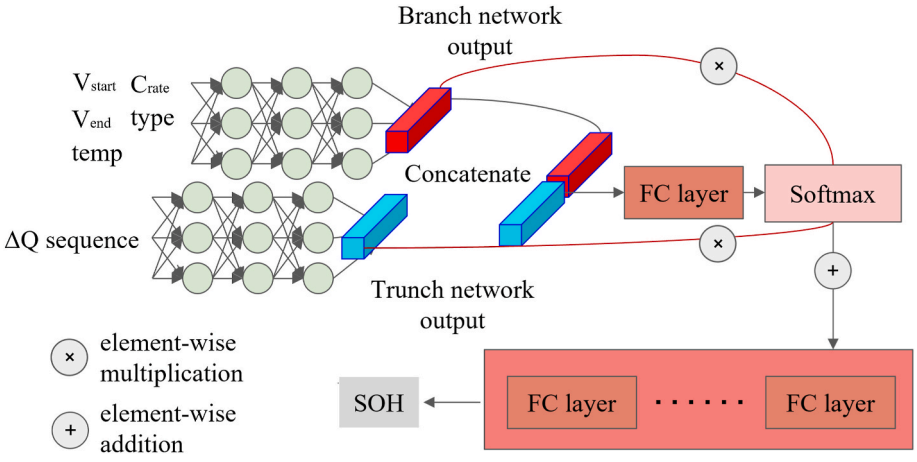


**Fig. 4.** A schematic representation of the AMFF-ONET module.

**Algorithm 2** (*continued*)

**Require:** $x_{\Delta Q}$: Input partial incremental capacity sequence, $[\Delta Q_1, \ldots, \Delta Q_{10}]$; $x_{cond}$: Input operating conditions, $[V_{start}, V_{end}, temp, C_{rate}, type]$.
**Ensure:** $SOH_{est}$: The estimated State of Health value.
**procedure** AMFF − ONET($x_{\Delta Q}, x_{cond}$)
*//Process inputs through branch end trunk networks*
$O_{trunk} \leftarrow TrunkNework(x_{\Delta Q})$ *//Get basis functions output*
$O_{branch} \leftarrow BranchNework(x_{cond})$ *//Get coefficients output*

*//Fuse outputs using the AMFF module*
$O_{concat} \leftarrow \text{Concatenate}(O_{trunk}, O_{branch})$
$V \leftarrow \tanh(\text{LinearLayer}(O_{concat}))$
$[w_1, w_2] \leftarrow \text{Softmax}(V)$ *//Generate two attention weights*

*//Apply attention weights and process through final layers*
$O_{weighted} \leftarrow w_1 \cdot O_{trunk} + w_2 \cdot O_{branch}$
$SOH_{est} \leftarrow \text{MultiLayerLinearModule}(O_{weighted})$ *//Process through*4 FC *layers*

**Return** $SOH_{est}$
**end procedure**

### 3.4. Resampling strategy for solving data imbalance

Existing studies have identified data imbalance as a critical issue in SOH estimation [57], stemming from the fundamentally nonlinear nature of battery aging processes. Take Dataset 1 as an example, the battery under 45 °C and 0.5C charging exhibits rapid capacity degradation during the initial 100 cycles, followed by a slower deterioration rate in subsequent cycles. As shown in Fig. S1, the nonlinear degradation rates result in an imbalanced distribution of data points among different SOH ranges, leading to compromised estimation performance.

A resampling is introduced to mitigate the aforementioned data imbalance phenomenon. During model training, the Probability Density Function (PDF) for each SOH interval (length = 0.01) is first computed based on the frequency of data points within that interval, and then performs weighted random sampling using inverse-PDF-derived weights, maintaining the original dataset size via replacement sampling.

### 3.5. Hyperparameter optimization

The tree-structured Parzen Estimator (TPE), an advanced Bayesian optimization algorithm with a tree-structured paradigm, was implemented to identify the optimal hyperparameters. Previous studies have demonstrated that TPE exhibits computational efficiency in high-dimensional parameter spaces. The hyperparameters of the framework are listed in Table 2.

The architectures of the branch network and trunk network are determined by combinations of two key hyperparameters: (1) the number of hidden units per layer, and (2) the depth of hidden layers. Following 200 iterations of TPE optimization, the optimal hyperparameter configurations for both ONET and AMFF-ONET models were identified through minimal validation loss, with detailed results documented in Tables 3 and 4, respectively.

### 3.6. Training strategy and experimental configuration

To prevent potential information leakage, the dataset was partitioned at the battery-cell level. For each sub-dataset, the number of batteries allocated to the training and validation sets was determined by selecting the nearest integers corresponding to a target ratio of 5:3:2, while all remaining batteries were assigned to the test set. For instance, a sub-dataset containing 7 batteries was divided into 3 training, 2 validation, and 2 test cells, respectively. In extreme cases with only 3 available cells, a 1:1:1 distribution was adopted to ensure that both the validation and test sets contained at least one unique, entirely unseen battery ID. This cell-wise partitioning strategy guarantees that no data windows from the evaluation units were ever encountered during the training process, providing a rigorous assessment of the model's robustness. To assess generalizability and reproducibility, multiple random seeds were employed for dataset partitioning. The estimation result is analyzed in the following section. The number of training epochs was set to 300. To mitigate overfitting, an early stopping strategy was implemented, wherein the model was saved only upon observing a reduction in validation error following each training iteration. The early stopping criterion was set with a patience threshold of 50 iterations to ensure robust convergence. A dynamic learning rate scheduling strategy was implemented, reducing the learning rate by half whenever the validation loss failed to decrease over ten consecutive epochs. A lower bound of $1 \times 10^{-8}$ was set for the learning rate. Root Mean Square Error (RMSE) was employed as the loss function for both training and validation. The overall training procedure is described in Algorithm 3.

The hardware used in our work was the 12th Gen Intel(R) Core (TM) i7-12700KF, 32 GB of memory, and NVIDIA GeForce GTX 1060 graphics card. The model was developed using Python 3.10 and implemented with PyTorch 2.10.

**Table 2**
Candidate hyperparameter configurations.

| Hyperparameter | Candidate values |
|---|---|
| Number of hidden units | 8, 16, 32, 64, 128 |
| Depth of the hidden layers | 2, 3, 4, 5 |
| Output size | 16, 32, 64, 128 |
| Learning rate | 0.01, 0.001, 0.0001 |
| is_resampling | 0, 1 |
| Batch size | 64, 128, 256, 512 |

**Table 3**
The optimal hyperparameters for ONET.

| Hyperparameter | Optimal value |
|---|---|
| Trunk network | [128, 128] |
| Branch network | [16,16,16,16,16] |
| Output size | 16 |
| Learning rate | 0.001 |
| is_resampling | 1 |
| Batch size | 128 |

**Table 4**
The optimal hyperparameters for AMFF-ONET.

| Hyperparameter | Optimal value |
|---|---|
| Trunk network | [58] |
| Branch network | [58] |
| Output size | 128 |
| Learning rate | 0.001 |
| is_resampling | 1 |
| Batch size | 512 |

**Algorithm 3**
Model Training Procedure

**Require:** $M$: An initialized model; $D_{train}$: Training Dataset; $D_{val}$: Validation Dataset; $E_{max}$: Maximum epochs; $P_{ES}$: Patience for early stopping; $P_{LR}$: Patience for learning rate reduction; *is_resampling*: Resampling flag
**Ensure:** $M_{best}$: The best trained model
**procedure** TRAINMODEL($M, D_{train}, D_{val}, \ldots$)
$L_{best} \leftarrow \infty$
$P_{ES\_count}, P_{LR\_count} \leftarrow 0, 0$
$M_{best} \leftarrow M$
**for** *epoch* $= 1 \rightarrow E_{max}$ **do**
**if** *is_resampling* **then**
$D'_{train} \leftarrow \text{Resample}(D_{train})$
**else**
$D'_{train} \leftarrow D_{train}$
**end if**
**for all** batch $(x, y)$ in $D'_{train}$ **do**

(*continued on next page*)

**Algorithm 3** (*continued*)

```
        ŷ ← M(x)
        loss ← RMSE(y, ŷ)
        Update M via backpropagation
    end for 16: L_val ← Evaluate(M, D_val)
    if L_val < L_best then
        L_best ← L_val
        M_best ← M
        P_ES_count, P_LR_count ← 0, 0
    else
        P_ES_count ← P_ES_count + 1
        P_LR_count ← P_LR_count + 1
    end if
    if P_LR_count ≥ P_LR then
        Halve the learning rate of M
        P_LR_count ← 0
    end if
    if P_ES_count ≥ P_ES then
        break
    end if
  end for 33: Return M_best
end procedure
```

### 3.7. Evaluation matrices

Three evaluation metrics (Mean Absolute Error (MAE), Root Mean Square Error (RMSE), Mean Absolute Percentage Error (MAPE), and $R^2$) were employed to assess the model's performance. The above three metrics were calculated using the following equations:

$$MAE = \frac{1}{n}\sum_{i=1}^{n}|y_i - \hat{y}_i|, \tag{5}$$

$$RMSE = \sqrt{\frac{1}{n}\sum_{i=1}^{n}(y_i - \hat{y}_i)^2}, \tag{6}$$

$$MAPE = \frac{1}{n}\frac{\sum_{i=1}^{n}\left|y_i - \hat{y}_i\right|}{y_i}, \tag{7}$$

$$R^2 = 1 - \frac{\sum_{i=1}^{n}(y_i - \hat{y}_i)^2}{\sum_{i=1}^{n}(y_i - \bar{y})^2}. \tag{8}$$

Where $n$ is the size of the test set, $y_i$ and $\hat{y}_i$ represent the ground-truth value and the predicted value for the $i^{th}$ sample, respectively. $\bar{y}$ denotes the mean value of $y$.

## 4. Results

This section presents a comparative analysis of the SOH estimation performance between ONET and AMFF-ONET.

### 4.1. Experimental results under different dataset splitting random seeds

To demonstrate the reproducibility of experiments, we evaluated estimation performance under different dataset splitting random seeds using 0.2 V-length $\Delta Q - V$ sequences. The experimental results are presented in Table 5. Furthermore, to verify that the evaluation result is not a byproduct of data redundancy from the sliding window protocol, a sensitivity analysis using a non-overlapping window strategy was conducted, with results presented in Table S6 of the Supplementary Material. Both ONET and AMFF-ONET demonstrate remarkable performance consistency across three different random seeds (2, 22, 42), confirming the experimental reproducibility of our framework. For subsequent analyses, the random seed is fixed at 42.

**Table 5**
Evaluation matrices obtained under different random seeds.

| Models | Random seed | MAE | RMSE | $R^2$ | MAPE |
|---|---|---|---|---|---|
| ONET | 2 | 0.00569 | 0.00810 | 0.985 | 0.00642 |
| | 22 | 0.00658 | 0.00970 | 0.978 | 0.00729 |
| | 42 | 0.00601 | 0.00864 | 0.982 | 0.00670 |
| AMFF-ONET | 2 | 0.00442 | 0.00636 | 0.990 | 0.00501 |
| | 22 | 0.00434 | 0.00614 | 0.991 | 0.00492 |
| | 42 | 0.00438 | 0.00617 | 0.991 | 0.00496 |

Two models demonstrate excellent predictive performance across all evaluation metrics (MAE, RMSE, and $R^2$). The ONET model achieves competitive performance, as evidenced by an $R^2$ coefficient of 0.982, complemented by MAE and RMSE values both below 0.9%. The enhanced AMFF-ONET model shows statistically superior performance, with MAE = 0.438%, RMSE = 0.617%, MAPE = 0.496%, and an improved $R^2$ of 0.991, representing a significant enhancement in estimation capability. Notably, these results were obtained on a comprehensive test set covering distinct battery chemistries and operating conditions, validating the models' remarkable capability for unified multi-scenario modeling.

Fig. 5 depicts the absolute error (AE) distributions of ONET and AMFF-ONET. The AE distributions of both models exhibit a strong concentration within the [0, 0.02] interval, accounting for 97.1% and 99.1% of the predictions, respectively. Meanwhile, while ONET achieves AEs below 1% in 82.6% of its predictions, the AMFF-ONET architecture significantly improves this high-accuracy proportion to 91.2%, representing a significant 10.4% improvement. The performance improvement between ONET and AMFF-ONET stems from their distinct fusion approaches - while ONET relies on inner product operations, the AMFF-ONET employs attention mechanisms to more effectively capture and weight degradation-relevant features in lithium-ion batteries.

### 4.2. Results on different sequence length

Table 6 presents the evaluation metrics for SOH estimation with three distinct $\Delta Q - V$ sequence lengths. Notably, the 0.1 V $\Delta Q - V$ sequence exhibits relatively good estimation accuracy, yielding MAE below 0.8%, RMSE under 1.2%, and $R^2$ greater than 0.969. All three metrics become better when the length of the $\Delta Q - V$ sequence increases. Meanwhile, AMFF-ONET consistently achieves greater estimation accuracy than ONET across all evaluated $\Delta Q - V$ sequence lengths. The above results demonstrate that the proposed framework shows robust performance with charging segments of different lengths, confirming its versatility in handling arbitrary charging sequences across different application scenarios. To achieve an optimal balance between estimation accuracy and practical applicability, the subsequent analysis employs 0.2 V length $\Delta Q - V$ sequences.

### 4.3. Results on different starting voltage

This subsection presents experimental results of the proposed models across varying starting voltage, which holds significant practical importance as it evaluates the models' robustness under different $\Delta Q - V$ sequences. The results, including MAE, RMSE, $R^2$, and data count, for both ONET and AMFF-ONET are exhibited in Fig. 6.

It is observed that both ONET and AMFF-ONET demonstrate excellent SOH estimation performance across different $\Delta Q - V$ sequences, with $R^2$ values consistently above 0.95, except for ONET in the 2.9 V-3.0 V range, which will be analyzed in the following paragraph. Meanwhile, the AMFF-ONET model demonstrates superior estimation performance compared to the ONET across all ranges for all three evaluation metrics. For example, the AMFF-ONET maintains MAE values below 0.5% within the 2.9 V to 3.8 V range, while achieving a peak $R^2$ of 0.994 between 3.4 V and 3.7 V. In contrast, the ONET only achieves MAE lower than 0.5% within the narrower range of 3.5 V to 3.6 V with a maximum $R^2$ of only

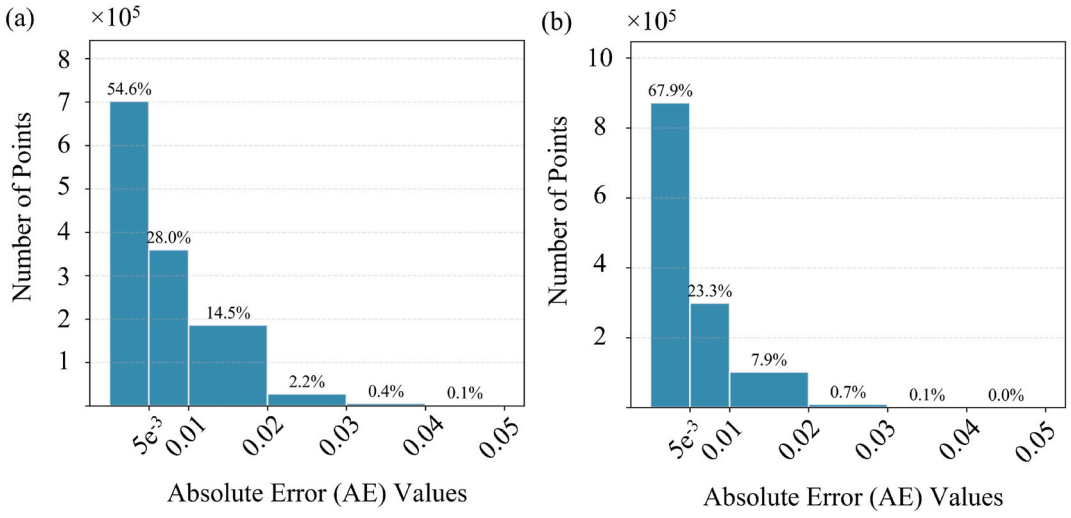


**Fig. 5.** AE distributions of ONET and AMFF-ONET.

**Table 6**
Evaluation results under different $\Delta Q - V$ sequence length.

| Sequence length | Model | MAE | RMSE | $R^2$ |
|---|---|---|---|---|
| 0.1 V | ONET | 0.00771 | 0.01148 | 0.969 |
| | AMFF-ONET | 0.00600 | 0.00904 | 0.981 |
| 0.15 V | ONET | 0.00712 | 0.01105 | 0.971 |
| | AMFF-ONET | 0.00494 | 0.00724 | 0.987 |
| 0.2 V | ONET | 0.00601 | 0.00864 | 0.982 |
| | AMFF-ONET | 0.00438 | 0.00617 | 0.991 |

0.991.

A particularly notable performance difference occurs in the 2.9 V-3.0 V range. While the ONET exhibits significantly degraded performance (MAE = 0.912%, RMSE = 1.1%), the AMFF-ONET maintains accurate estimation (MAE = 0.424%, RMSE = 0.556%, $R^2$ = 0.958). This performance discrepancy can be attributed to the limited data set, which includes only 238 test data points in this voltage range, as shown in Fig. 6(d). Such a small data size adversely affects ONET's estimation accuracy, whereas it exerts merely a negligible influence on AMFF-ONET's performance. The enhanced performance of the AMFF-ONET can be attributed to the AMFF attention module, which compensates for data limitations while maintaining high estimation accuracy. This demonstrates the attention module's critical role in improving both the accuracy and robustness of SOH estimation.

Both models exhibit a noticeable performance degradation when the starting voltage exceeds 3.7 V. This phenomenon can be explained by the analysis presented in Fig. S2, which plots $\Delta Q - V$ curves at different starting voltages. When the starting voltage is set at 3.6 V and 3.7 V, the $\Delta Q - V$ curves exhibit excellent distinguishability across different cycles. However, this discrimination significantly diminishes at higher starting voltages, where the $\Delta Q - V$ curves from varying cycles starting

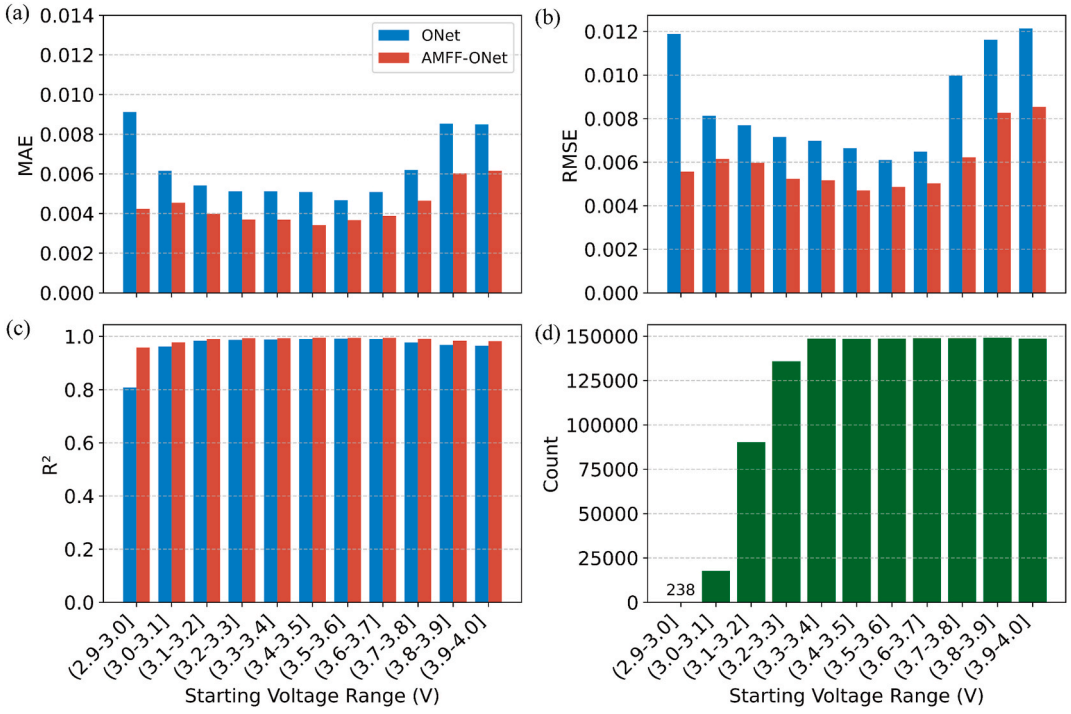


**Fig. 6.** Experimental results across different voltage ranges: (a) MAE, (b) RMSE, (c) $R^2$, and (d) distribution of test data points.

at 3.85 V and 3.95 V become indistinguishable, clustering within a narrow range. The minimal discernible differences between these curves account for the observed performance decline in these voltage ranges. It is noted that the AMFF-ONET maintains superior estimation accuracy even under these challenging conditions, demonstrating exceptional performance metrics: a maximum MAE of 0.614%, RMSE of 0.854%, while maintaining an $R^2$ value of 0.983. These results further demonstrate the robustness and excellence of the AMFF-ONET architecture.

### 4.4. Results on different SOH

In this subsection, the proposed models are tested under different SOH values to ensure robust estimation performance throughout the entire battery life. The results are plotted in Fig. 7. Since the variance of ground-truth SOH values within the range is negligible, $R^2$ is not employed as the evaluation metric. Consistent with the results at varying starting voltages, AMFF-ONET achieves superior predictive performance over ONET, with MAE consistently below 0.55% across all SOH ranges. In contrast, ONET shows significant performance fluctuations: at high SOH ($>$ 0.99), its MAE (0.922%) and RMSE (1.37%) reflect degradations of 83.3% and 90.5%, respectively, relative to its optimal performance in the (0.76, 0.77] interval.

It is noted that ONET exhibits significant performance fluctuations, particularly the RMSE surge observed in the (0.82-0.83] SOH range, whereas it maintains consistent MAE values. This divergence suggests its sensitivity to a limited number of "highly deviant estimation outliers". This suggests that the simple inner product fusion mechanism is less robust to unusual data points within certain SOH regions. In contrast, the AMFF-ONET model maintains consistent and superior performance across all SOH ranges, demonstrating its enhanced robustness. This improvement is directly attributable to the AMFF module. By replacing the inner product with an attention mechanism, the model can weight features from the trunk and branch networks, mitigating the influence of outliers and adapting to the varying information content of features at different SOH levels. The subsequent multi-layer linear transformation further enhances its nonlinear modeling capability, ensuring robust and accurate estimations throughout the battery's entire lifecycle.

### 4.5. Results on different battery material

While prior studies typically rely on transfer learning to enable cross-battery-type SOH estimation, the proposed ONET and AMFF-ONET architectures directly embed battery type information as model inputs, eliminating the need for transfer learning while maintaining estimation accuracy across diverse battery chemistries. Comparative estimation results for NCA and NCM battery chemistries are summarized in Table 7.

AMFF-ONET maintains consistent performance across the different chemistries integrated within the unified framework: MAE increased marginally from 0.429% to 0.448% (+4.7%), RMSE rose from 0.579% to 0.662% (+13.8%), while $R^2$ changed from 0.992 to 0.990. This minimal performance deviation confirms the model's effectiveness in capturing chemistry-specific degradation features within a single operator mapping. In contrast to AMFF-ONET's consistent performance, ONET demonstrates significantly higher estimation errors in NCM batteries, yielding an RMSE value greater than 1%, revealing its limited adaptability to this chemistry-specific degradation behavior.

### 4.6. Computational load analysis

The detailed results are shown in Table 8, which demonstrates the model's efficiency in real-world deployment scenarios. To evaluate the computational efficiency of our proposed model, we performed an assessment using the following key metrics: parameter count, model size, prediction time per sample, and memory usage. The prediction time was determined by computing the mean execution duration across 1000 consecutive forward passes. To ensure statistical reliability, this evaluation protocol was repeated in ten independent trials, and the final performance metrics represent the ensemble averages across all experimental repetitions.

It is noted that ONET exhibits computational efficiency and lightweight architecture, where the inner product operation serves as a computationally economical aggregation mechanism. Compared to ONET, the AMFF-ONET model has twice the model size of ONET,

**Table 7**
Evaluation results across different battery types.

| Model | Battery type | MAE | RMSE | $R^2$ |
|---|---|---|---|---|
| ONET | NCA | 0.00534 | 0.00709 | 0.988 |
| | NCM | 0.00685 | 0.01028 | 0.976 |
| AMFF-ONET | NCA | 0.00429 | 0.00579 | 0.992 |
| | NCM | 0.00448 | 0.00662 | 0.990 |

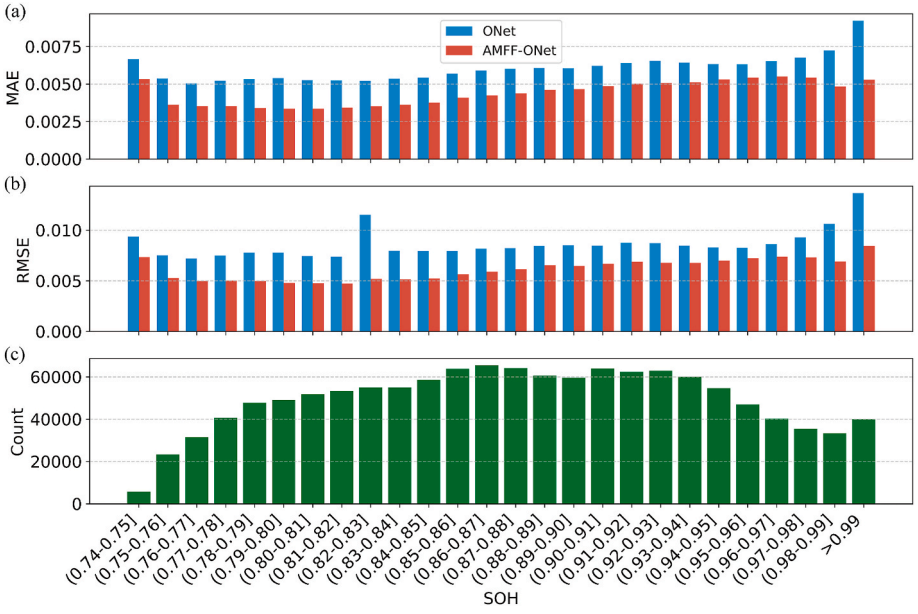


**Fig. 7.** Experimental results across different SOH: (a) MAE, (b) RMSE, and (c) distribution of test data points.

**Table 8**
Model parameter count, size, and estimation time.

| Model | Parameter count | Model size (KB) | Estimation time (ms/sample) |
|---|---|---|---|
| ONET | 21440 | 91.7 | 0.41 |
| AMFF-ONET | 55683 | 229 | 0.61 |

reflecting the additional parameters required by the attention mechanism. However, the introduction of the attention module also enhances the SOH estimation accuracy and robustness, as evidenced by the above experimental results. Although AMFF-ONET requires higher computational costs than ONET, it remains highly lightweight compared to other SOH estimation models. With a compact model size of 229 KB, it occupies only 11.3% of the memory footprint of the reference edge-computing model in Ref. [38]. This footprint is well within the Flash memory constraints of mainstream automotive-grade microcontrollers, such as the ARM Cortex-M series, which typically offer 512 KB to 2 MB of storage [59]. Furthermore, the inference latency of 0.61 ms is significantly shorter than the typical Battery Management System (BMS) control cycle of 10-100 ms, ensuring that SOH estimation can be executed in real-time without disrupting high-priority safety functions [60,61]. Consequently, the framework effectively addresses the hardware limitations of resource-constrained edge devices while maintaining high-frequency monitoring capabilities.

The above results demonstrate that ONET and AMFF-ONET achieve a balance between efficiency and estimation performance. With inference latencies consistently below 1 ms with the NVIDIA GeForce GTX 1060 graphics card, the proposed framework sufficiently meets the stringent real-time requirements for battery management systems, enabling high-frequency SOH monitoring. Besides, the compact model size ensures easy deployment on resource-constrained edge devices. This combination of lightweight and computational efficient design renders ONET and AMFF-ONET suitable for edge systems.

### 4.7. Comparison with other AI-driven models

The corresponding parameter settings of model benchmarking with other methods are provided in Supplementary Note S1. The comparative results are detailed in Table 9.

The proposed framework demonstrates competitive accuracy that is comparable to other AI-driven approaches. Specifically, AMFF-ONET achieves performance metrics that closely align with those of the state-of-the-art (SOTA) R-TNet model, showing differences of just 0.00064 in RMSE and 0.00024 in MAE. In addition, AMFF-ONET achieves a higher $R^2$ value than R-TNet (0.991 versus 0.990). Furthermore, no other models achieve SOH estimation across different battery chemistries without transfer learning.

**Table 9**
Advanced SOH estimation model performance comparison.

| Models | RMSE | MAE | R 2 | Battery type |
|---|---|---|---|---|
| CNN [62] | 0.0089 | 0.0061 | 0.9845 | NCM |
| CNN-FT [63] | 0.0128 | – | 0.9492 | NCM |
| QCNN [64] | 0.00653 | 0.00474 | 0.988 | NCA |
| | 0.0093 | 0.00654 | 0.971 | NCM |
| PINN [58] | 0.0158 | – | – | NCA |
| | 0.0132 | – | – | NCM |
| R-Tnet [50] | 0.00553 | 0.00414 | 0.99 | NCA |
| TSPINN [65] | – | 0.0068 | – | NCA |
| | – | 0.0067 | – | NCM |
| ONET | 0.00864 | 0.00601 | 0.982 | NCA NCM |
| AMFF-ONET | 0.00617 | 0.00438 | 0.991 | NCA NCM |
| ONET (evaluated under [3.55 V, 3.94 V]) | 0.00859 | 0.00611 | 0.983 | NCA NCM |
| AMFF-ONET (evaluated under [3.55 V, 3.94 V]) | 0.00604 | 0.00429 | 0.991 | NCA NCM |

It is important to acknowledge that the benchmark models and our proposed framework were evaluated under different experimental settings, which may influence direct numerical comparisons. For instance, several benchmark models were exclusively tested within limited, highly SOH-sensitive voltage windows (e.g., [3.55 V, 3.94 V]) [50]. To mitigate potential methodological bias and ensure a rigorous comparison, we implemented measures by re-evaluating our framework specifically on the high-sensitivity voltage segment ([3.55 V, 3.94 V]) utilized by the R-Tnet baseline. The quantitative results reveal that AMFF-ONET achieves an MAE of 0.00429, an RMSE of 0.00604, and an $R^2$ of 0.991 on this specific window. This performance is not only consistent with our randomized full-range evaluation but also remains highly competitive against the SOTA R-Tnet. Crucially, while R-Tnet and other benchmarks are typically optimized for single-chemistry datasets, AMFF-ONET maintains this high precision within a unified dual-chemistry framework (NCA and NCM) without the need for chemistry-specific fine--tuning or transfer learning. These results demonstrate that AMFF-ONET achieves superior accuracy across both the full constant-current charging profile and the specific high-sensitivity voltage range, thereby establishing its exceptional precision and robust performance within a unified multi-condition framework.

### 4.8. Evaluation of model robustness against Gaussian Noise

In this subsection, to evaluate the robustness of the proposed framework, we conducted an immunity test against Gaussian noise. Zero-mean Gaussian noise with different standard deviations was introduced into the input $\Delta Q$ sequences to simulate varying levels of sensor noise in real-world applications. The experimental results for ONET and AMFF-ONET are presented in Fig. 1, respectively.

As depicted in Fig. 8, both models exhibit a significant degradation in performance with increasing noise intensity (i.e., decreasing SNR), demonstrating the inherent challenge posed by sensor noise. While both MAE and RMSE escalate for each model, the AMFF-ONET consistently maintains a modest advantage in these error metrics. For instance, under the most severe noise condition (SNR = 30 dB), the AMFF-ONET achieves an MAE of 0.0205 and an RMSE of 0.031, which are respectively 10.9% and 8.8% lower than the conventional ONET's MAE of 0.023 and RMSE of 0.034.

However, this relatively small improvement in absolute error values underscores a more critical divergence in model fidelity under noisy conditions, which is most starkly revealed by the $R^2$ Fig. 8(c). While both models deliver similar, high-fidelity performance at high SNRs ($\geq$ 45 dB), a pronounced and rapid performance decline becomes evident as the SNR falls. At 35 dB, the $R^2$ for the conventional ONET exhibits a precipitous decline to 0.86, a trend that culminates in a severe collapse to just 0.67 at 30 dB. In contrast, the AMFF-ONET, while not immune to noise-induced degradation, demonstrates markedly greater resilience, sustaining an $R^2$ of 0.90 at 35 dB and retaining a substantially higher score of 0.78 even at the extreme noise level of 30 dB. At this point, the AMFF-ONET's $R^2$ is 16.4% higher than that of the conventional ONET, signifying a critical preservation of its estimation performance and a mitigation of catastrophic failure modes observed in the baseline.

This enhanced robustness and superior noise tolerance are primarily attributed to the AMFF module's attention mechanism. This mechanism dynamically re-weights features to effectively suppress noise artifacts and amplify the salient degradation signatures within the corrupted $\Delta Q$ sequences, thus preventing a disproportionate degradation in predictive power. However, it is crucial to acknowledge that the current framework does not integrate dedicated modules specifically designed for advanced noise suppression or robust feature learning in the presence of strong perturbations. Consequently, while outperforming the baseline, the absolute level of noise immunity in AMFF-ONET, particularly under very low SNR conditions, still presents avenues for further improvement.

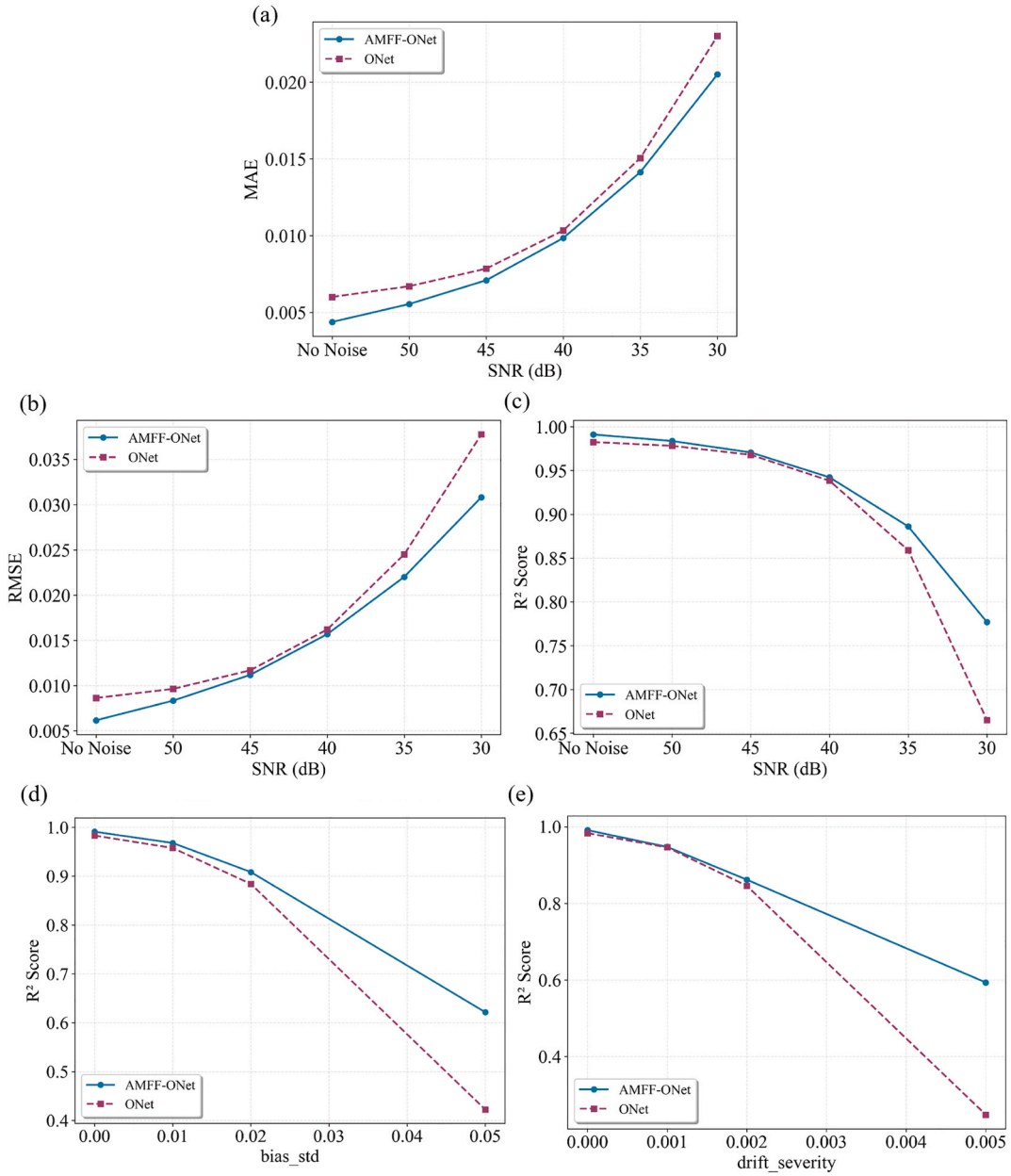


**Fig. 8.** Evaluation results against Gaussian Noise with varying SNRs: (a) MAE, (b) RMSE, and (c) $R^2$. And evaluation results under realistic BMS conditions: (d) $R^2$ scores under different levels of current sensor bias, and (e) $R^2$ scores under varying intensities of integration drift.

To further evaluate the model's resilience under realistic BMS conditions, we extended the robustness analysis to include current sensor bias and integration drift. Fig. 8(d) illustrates the impact of current bias, where the input $\Delta Q$ features undergo linear scaling. While the performance of the ONet degrades rapidly as the bias standard deviation (*bias_std*) increases, AMFF-ONet maintains a significantly higher $R^2$ score, staying above 0.6 even at a 5% bias level. Similarly, Fig. 8(e) shows the results under varying integration drift (*drift_severity*). AMFF-ONet demonstrates superior stability, whereas the baseline ONet's performance drops sharply. The robustness of AMFF-ONet stems from the attention mechanism, which effectively prioritizes stable electrochemical signatures, and the use of short 0.2 V windows that inherently limit the time interval for error accumulation. These results confirm that the proposed framework is well-suited for non-ideal sensing environments in practical energy storage infrastructures.

Collectively, these results provide compelling quantitative evidence that the AMFF-ONET, despite inherent challenges of noisy data and without specialized noise-robust architectural components, not only achieves higher accuracy but also possesses significantly superior robustness compared to the conventional ONET. This makes it a critical attribute for reliable deployment in practical BMS where measurement noise is an operational reality, though future work will explore the integration of explicit noise-robust enhancements to further elevate its performance in highly noisy environments.

### 4.9. Discussion about ONET and AMFF-ONET

As elaborated in the following subsections, AMFF-ONET demonstrates superior estimation performance compared to ONET. Across diverse $\Delta Q - V$ sequences, battery chemistries, and different Gaussian noise intensities, AMFF-ONET consistently outperforms ONET in all evaluation metrics. Since the architectural difference lies solely in the fusion module, we attribute this performance enhancement to the introduced AMFF mechanism. The AMFF module replaces the conven-

tional inner product operation with an attention-based weighted summation that dynamically evaluates the importance of both the Branch and Trunk network outputs, followed by four fully connected layers for final SOH inference. While AMFF module slightly increases computational burden, AMFF-ONET remains an exceptionally compact model size and efficient inference time. These results demonstrate that AMFF-ONET is more suited for practical BMS implementations than ONET, particularly in edge computing where both accuracy and efficiency are critical.

Beyond accuracy and efficiency, the trunk-branch decomposition of the ONET architecture offers inherent interpretability advantages for understanding battery aging. Mathematically, the framework approximates the SOH estimation through a combination of basis functions and their corresponding coefficients. The trunk network effectively extracts universal degradation basis functions that represent intrinsic degradation patterns from partial $\Delta Q$ sequences. Concurrently, the branch network acts as a condition-dependent modulator, learning how operational conditions weight these basis functions. Although the branch inputs (e.g., temperature and charging rate) are static, the trunk network processes the sequential voltage-capacity evolution, allowing the framework to capture the time-coupled aging dynamics through the nonlinear interaction between the two sub-networks. This decoupling allows for a more transparent understanding of state estimation, as it explicitly reveals how external operation conditions influence the fundamental modes of capacity loss. Such a structure shifts the model from a pure 'black-box' toward a more interpretable 'grey-box' paradigm, providing researchers with insights into the conditional dependencies of battery health.

To distinguish whether the observed robustness stems from the short-window preprocessing or the architecture itself, it is emphasized that while the 0.2 V window protocol functions as a feature extraction filter to enhance local sensitivity, it is not the sole driver of performance. As demonstrated in the comparative study (Section 4.7), baseline models employing the identical data protocol exhibit significantly higher error variance under fluctuating temperatures. This suggests that while the data protocol ensures a high-quality input signal, the ONet architecture functions as a robust operator mapper that effectively decouples condition-dependent perturbations from the underlying aging trajectory. This distinction confirms that the model's superiority is fundamentally rooted in its operator-learning design rather than being a mere artifact of data windowing.

## 5. Conclusion

This paper addressed the critical challenge in SOH estimation: the absence of a unified, lightweight framework that can generalize across diverse operational conditions. By reformulating SOH estimation as an operator learning problem, this work presents an ONET-based model that meets all of the above-mentioned demands. The proposed framework, built on an ONET architecture, successfully decouples the degradation mapping (via a trunk network) from the operational conditions (via a branch network). By incorporating the idea of operator learning, the model directly accepts operational conditions and chemistries as input, enabling more flexible and generalized SOH estimation under varying scenarios without transfer learning strategies. The integration of the AMFF module proved crucial, significantly enhancing estimation accuracy and robustness over the standard ONET and achieving a MAE of 0.438%, a MAPE of 0.496%, and an $R^2$ of 0.991 on a challenging dual-chemistry multi-condition dataset using arbitrary 0.2 V charging segments. With a compact model size under 230 KB, the framework is exceptionally well-suited for deployment on resource-constrained BMS. Ultimately, this work constitutes the first application of a nonlinear operator learning paradigm to battery SOH estimation, offering a promising pathway for developing the next generation of unified and efficient energy storage diagnostics. The proposed framework offers several key advantages. It achieves accurate and robust SOH estimation using only a short 0.2 V $\Delta Q - V$ sequence, making it highly practical for real-world scenarios. This practicality is further enhanced by its end-to-end architecture, which boosts efficiency by eliminating the need for complex feature preprocessing. More importantly, by directly embedding operating conditions and battery type as model inputs, the framework can generalize its accurate estimations across diverse operating scenarios and battery chemistries. Moreover, these capabilities are packaged in a lightweight architecture, with a model size of 230 KB that enables practical deployment on resource-constrained edge devices.

Despite the promising results, this study has several limitations that open avenues for future research. First, our analysis in Section 4.3 revealed a performance degradation when the charging segments were extracted from high voltage ranges. This can be attributed to the diminished distinguishability of $\Delta Q - V$ curves in these regions across aging cycles, which provides fewer degradation-related features for the model to learn from. Future work could focus on developing feature fusion mechanisms, integrating data from differential voltage analysis or other sensitive parameters to compensate for the lack of information in these high-voltage segments. Second, while the AMFF-ONET demonstrated strong robustness across input $\Delta Q$ sequences, the base ONET model showed suboptimal performance in specific data-scarce regions and at high SOH levels. This indicates that the model's stability is susceptible to imbalanced data distributions. To address this, future improvements could involve incorporating physics-informed neural networks (PINNs) to better constrain model estimations in data-sparse regions or employing generative models for data augmentation. Third, the proposed framework's scalability to a much larger set of operating conditions (e.g., battery chemistries, wider temperature ranges, various discharge protocols) remains to be explored. As noted, excessive input dimensions to the branch network could introduce challenges in hyperparameter tuning. Therefore, a key direction for future research will be to enhance the branch network's architecture, for instance, by integrating graph neural networks or specialized attention mechanisms capable of effectively modeling the complex interactions between a microscopic degradation evolution and macroscopic changes. Furthermore, while the current study utilizes segments from the constant-current charging phase due to its prevalence in standard charging protocols, the proposed ONET-based framework holds significant potential for dynamic or mixed charging profiles. The fundamental advantage of operator learning lies in its ability to approximate continuous mappings, allowing the model to handle input sequences of arbitrary temporal resolution and length. In real-world applications where charging might be intermittent or involve variable currents (e.g., regenerative braking or opportunistic charging), the ONET architecture can be further adapted by embedding the instantaneous current profiles into the branch network as conditioning parameters. Future work will explore the integration of such dynamic operational data to further enhance the versatility of the framework in unpredictable real-world environments. Finally, beyond the operational flexibility, the unified architecture and consistent performance across different chemistries of the AMFF-ONET provide a promising foundation for the health management of second-life batteries. In these scenarios, where diverse aging histories and heterogeneous battery chemistries necessitate adaptive yet lightweight monitoring solutions, the proposed framework could significantly facilitate safe and efficient battery repurposing in large-scale energy storage systems.

## CRediT authorship contribution statement

**Hang Hu:** Investigation. **Chen Liang:** Formal analysis. **Xinghao Huang:** Formal analysis. **Huadong Mo:** Investigation. **Changfu Zou:** Project administration. **Shengyu Tao:** Resources, Project administration, Methodology, Investigation, Funding acquisition, Formal analysis, Data curation, Conceptualization.

## Declaration of competing interest

The authors declare that they have no known competing financial interests or personal relationships that could have appeared to influence the work reported in this paper.

## Acknowledgement

This work was supported by the Hebei Provincial Key Research Projects (23281901Z), the Swedish Research Council through a Project Grant (Grant No. 2023-04314) and the European Union's Horizon Europe programme through the Marie Skłodowska-Curie Actions (Grant No. 101131278).

## Appendix A. Supplementary data

Supplementary data to this article can be found online at https://doi.org/10.1016/j.jpowsour.2026.239592.

## Data availability

The data for the modeling work used in this work can be found at [54]. Other data are all available in the manuscript.

## References

[1] K. Yang, L. Zhang, Z. Zhang, H. Yu, W. Wang, M. Ouyang, et al., Battery state of health estimate strategies: from data analysis to end-cloud collaborative framework, Batteries 9 (2023), https://doi.org/10.3390/batteries9070351.
[2] K. Liu, Z. Wei, C. Zhang, Y. Shang, R. Teodorescu, Q.-L. Han, Towards long lifetime battery: AI-based manufacturing and management, IEEE/CAA Journal of Automatica Sinica 9 (2022) 1139–1165, https://doi.org/10.1109/JAS.2022.105599.
[3] S. Wang, C. Ma, H. Gao, D. Deng, C. Fernandez, F. Blaabjerg, Improved hyperparameter Bayesian optimization-bidirectional long short-term memory optimization for high-precision battery state of charge estimation, Energy 328 (2025) 136598, https://doi.org/10.1016/j.energy.2025.136598.
[4] S. Wang, H. Gao, P. Takyi-Aninakwa, J.M. Guerrero, C. Fernandez, Q. Huang, Improved multiple feature-electrochemical thermal coupling modeling of lithium-ion batteries at low-temperature with real-time coefficient correction, Protection and Control of Modern Power Systems 9 (2024) 157–173, https://doi.org/10.23919/PCMP.2023.000257.
[5] L. Tong, Y. Li, Y. Xu, J. Fang, C. Wen, Y. Zheng, et al., A combined method for state-of-charge estimation for lithium-ion batteries based on IGWO-ASRCKF and ELM under various aging levels, J. Energy Storage 124 (2025) 116843, https://doi.org/10.1016/j.est.2025.116843.
[6] H. Ruan, J.V. Barreras, T. Engstrom, Y. Merla, R. Millar, B. Wu, Lithium-ion battery lifetime extension: a review of derating methods, J. Power Sources 563 (2023) 232805, https://doi.org/10.1016/j.jpowsour.2023.232805.
[7] S. Wang, Y. Fan, S. Jin, P. Takyi-Aninakwa, C. Fernandez, Improved anti-noise adaptive long short-term memory neural network modeling for the robust remaining useful life prediction of lithium-ion batteries, Reliab. Eng. Syst. Saf. 230 (2023) 108920, https://doi.org/10.1016/j.ress.2022.108920.
[8] C. Lin, J. Xu, D. Jiang, J. Hou, Y. Liang, Z. Zou, et al., Multi-model ensemble learning for battery state-of-health estimation: recent advances and perspectives, J. Energy Chem. 100 (2025) 739–759, https://doi.org/10.1016/j.jechem.2024.09.021.
[9] Z. Ren, C. Du, A review of machine learning state-of-charge and state-of-health estimation algorithms for lithium-ion batteries, Energy Rep. 9 (2023) 2993–3021, https://doi.org/10.1016/j.egyr.2023.01.108.
[10] K. Luo, X. Chen, H. Zheng, Z. Shi, A review of deep learning approach to predicting the state of health and state of charge of lithium-ion batteries, J. Energy Chem. 74 (2022) 159–173, https://doi.org/10.1016/j.jechem.2022.06.049.
[11] Y. Chen, W. Duan, Y. He, S. Wang, C. Fernandez, A hybrid data driven framework considering feature extraction for battery state of health estimation and remaining useful life prediction, Green Energy Intell. Transp. 3 (2024) 100160, https://doi.org/10.1016/j.geits.2024.100160.
[12] P. Ding, T. Li, Y. Qiao, L. Zheng, H. Deng, W. Wu, Integrated framework for battery SOH estimation using incremental capacity and image feature transformation, Green Energy Intell. Transp. (2025) 100366, https://doi.org/10.1016/j.geits.2025.100366.
[13] J. Wang, Z. Deng, T. Yu, A. Yoshida, L. Xu, G. Guan, et al., State of health estimation based on modified gaussian process regression for lithium-ion batteries, J. Energy Storage 51 (2022) 104512, https://doi.org/10.1016/j.est.2022.104512.
[14] W.W. Xing, A.A. Shah, N. Shah, Y. Wu, Q. Xu, A. Rodchanarowan, et al., Data-driven prediction of Li-Ion battery degradation using predicted features, Processes 11 (2023), https://doi.org/10.3390/pr11030678.
[15] D. Yang, X. Zhang, R. Pan, Y. Wang, Z. Chen, A novel Gaussian process regression model for state-of-health estimation of lithium-ion battery using charging curve, J. Power Sources 384 (2018) 387–395, https://doi.org/10.1016/j.jpowsour.2018.03.015.
[16] M. Xu, Y. Liu, C. Yue, J. Yu, W. Chen, X. Zhou, Battery state-of-health prediction using a novel enhanced sparse variational gaussian process framework, Green Energy Intell. Transp. (2025) 100374, https://doi.org/10.1016/j.geits.2025.100374.
[17] T. Tao, C. Ji, J. Dai, J. Rao, J. Wang, W. Sun, et al., Data-based health indicator extraction for battery SOH estimation via deep learning, J. Energy Storage 78 (2024) 109982, https://doi.org/10.1016/j.est.2023.109982.
[18] P. Ding, M. Xia, X. Wang, H. Pan, Q. Gao, W. Guo, et al., Advanced lithium-ion battery health state estimation using a Bayesian optimization hybrid neural network model, J. Energy Storage 123 (2025) 116562, https://doi.org/10.1016/j.est.2025.116562.
[19] S. Peng, Y. Wang, A. Tang, Y. Jiang, J. Kan, M. Pecht, State of health estimation joint improved grey wolf optimization algorithm and LSTM using partial discharging health features for lithium-ion batteries, Energy 315 (2025) 134293, https://doi.org/10.1016/j.energy.2024.134293.
[20] C. Zhang, L. Luo, Z. Yang, S. Zhao, Y. He, X. Wang, et al., Battery SOH estimation method based on gradual decreasing current, double correlation analysis and GRU, Green Energy Intell. Transp. 2 (2023) 100108, https://doi.org/10.1016/j.geits.2023.100108.
[21] Z. Xu, Z. Chen, L. Yang, S. Zhang, State of health estimation for lithium-ion batteries based on incremental capacity analysis and transformer modeling, Appl. Soft Comput. 165 (2024) 112072, https://doi.org/10.1016/j.asoc.2024.112072.
[22] S. Tao, R. Ma, Y. Chen, Z. Liang, H. Ji, Z. Han, et al., Rapid and sustainable battery health diagnosis for recycling pretreatment using fast pulse test and random forest machine learning, J. Power Sources 597 (2024) 234156, https://doi.org/10.1016/j.jpowsour.2024.234156.
[23] M. Lin, D. Wu, J. Meng, J. Wu, H. Wu, A multi-feature-based multi-model fusion method for state of health estimation of lithium-ion batteries, J. Power Sources 518 (2022) 230774, https://doi.org/10.1016/j.jpowsour.2021.230774.
[24] B. Zhang, W. Liu, Y. Cai, Z. Zhou, L. Wang, Q. Liao, et al., State of health prediction of lithium-ion batteries using particle swarm optimization with levy flight and generalized opposition-based learning, J. Energy Storage 84 (2024) 110816, https://doi.org/10.1016/j.est.2024.110816.
[25] K. Chen, J. Li, K. Liu, C. Bai, J. Zhu, G. Gao, et al., State of health estimation for lithium-ion battery based on particle swarm optimization algorithm and extreme learning machine, Green Energy Intell. Transp. 3 (2024) 100151, https://doi.org/10.1016/j.geits.2024.100151.
[26] W. Liu, J. Tian, X. Li, Y. Tian, G. Li, A Fourier graph neural network for SOH estimation of lithium-ion batteries simultaneously considering spatio-temporal features, Green Energy Intell. Transp. 5 (2026) 100301, https://doi.org/10.1016/j.geits.2025.100301.
[27] W. Li, N. Sengupta, P. Dechent, D. Howey, A. Annaswamy, D.U. Sauer, Online capacity estimation of lithium-ion batteries with deep long short-term memory networks, J. Power Sources 482 (2021) 228863, https://doi.org/10.1016/j.jpowsour.2020.228863.
[28] C. Jia, Y. Tian, Y. Shi, J. Jia, J. Wen, J. Zeng, State of health prediction of lithium-ion batteries based on bidirectional gated recurrent unit and transformer, Energy 285 (2023) 129401, https://doi.org/10.1016/j.energy.2023.129401.
[29] Z. Wang, X. Zhao, D. Zhen, J. Pombo, W. Yang, F. Gu, et al., Adaptable capacity estimation of lithium-ion battery based on short-duration random constant-current charging voltages and convolutional neural networks, Energy 306 (2024) 132541, https://doi.org/10.1016/j.energy.2024.132541.
[30] C. Qian, B. Xu, L. Chang, B. Sun, Q. Feng, D. Yang, et al., Convolutional neural network based capacity estimation using random segments of the charging curves for lithium-ion batteries, Energy 227 (2021) 120333, https://doi.org/10.1016/j.energy.2021.120333.
[31] J. Tian, R. Xiong, W. Shen, J. Lu, F. Sun, Flexible battery state of health and state of charge estimation using partial charging data and deep learning, Energy Storage Mater. 51 (2022) 372–381, https://doi.org/10.1016/j.ensm.2022.06.053.
[32] K. Zhang, S.K. Rayeem, W. Mai, J. Tian, L. Ma, T. Zhang, et al., Enhancing battery health estimation using incomplete charging curves and knowledge-guided deep learning, Reliab. Eng. Syst. Saf. (2025) 111211, https://doi.org/10.1016/j.ress.2025.111211.
[33] Y. Liu, G. Fan, B. Zhou, S. Chen, Z. Sun, Y. Wang, et al., Rapid and flexible battery capacity estimation using random short-time charging segments based on residual convolutional networks, Appl. Energy 351 (2023) 121925, https://doi.org/10.1016/j.apenergy.2023.121925.
[34] Y. Xiang, W. Fan, J. Zhu, X. Wei, H. Dai, Semi-supervised deep learning for lithium-ion battery state-of-health estimation using dynamic discharge profiles, Cell Rep. Phys. Sci. 5 (2024) 101763, https://doi.org/10.1016/j.xcrp.2023.101763.
[35] J. Tian, R. Xiong, W. Shen, J. Lu, X.-G. Yang, Deep neural network battery charging curve prediction using 30 points collected in 10 min, Joule 5 (2021) 1521–1534, https://doi.org/10.1016/j.joule.2021.05.012.
[36] M. Lin, L. Ke, J. Meng, W. Wang, J. Wu, F. Wang, Health status estimation of lithium-ion battery under arbitrary charging voltage information using ensemble learning framework, Reliab. Eng. Syst. Saf. 256 (2025) 110782, https://doi.org/10.1016/j.ress.2024.110782.
[37] L. Zhang, J. Zhang, T. Gao, L. Lyu, L. Wang, W. Shi, et al., Improved LSTM based state of health estimation using random segments of the charging curves for lithium-ion batteries, J. Energy Storage 74 (2023) 109370, https://doi.org/10.1016/j.est.2023.109370.

[38] J. Chen, P. Kollmeyer, R. Ahmed, A. Emadi, Battery state-of-health estimation using CNNs with transfer learning and multi-modal fusion of partial voltage profiles and histogram data, Appl. Energy 391 (2025) 125923, https://doi.org/10.1016/j.apenergy.2025.125923.
[39] W. Sun, C. Wu, C. Xie, X. Wang, Y. Guo, Y. Tang, et al., Fine-tuning enables state of health estimation for lithium-ion batteries via a time series foundation model, Energy 318 (2025) 134177, https://doi.org/10.1016/j.energy.2024.134177.
[40] A. Tang, Y. Xu, Y. Hu, J. Tian, Y. Nie, F. Yan, et al., Battery state of health estimation under dynamic operations with physics-driven deep learning, Appl. Energy 370 (2024) 123632, https://doi.org/10.1016/j.apenergy.2024.123632.
[41] A. Tang, Y. Jiang, Y. Nie, Q. Yu, W. Shen, M.G. Pecht, Health and lifespan prediction considering degradation patterns of lithium-ion batteries based on transferable attention neural network, Energy 279 (2023) 128137, https://doi.org/10.1016/j.energy.2023.128137.
[42] J. Zhao, Z. Wang, Y. Wu, A.F. Burke, Predictive pretrained transformer (PPT) for real-time battery health diagnostics, Appl. Energy 377 (2025) 124746, https://doi.org/10.1016/j.apenergy.2024.124746.
[43] H. Ruan, Z. Wei, W. Shang, X. Wang, H. He, Artificial Intelligence-based health diagnostic of Lithium-ion battery leveraging transient stage of constant current and constant voltage charging, Appl. Energy 336 (2023) 120751, https://doi.org/10.1016/j.apenergy.2023.120751.
[44] S. Sahoo, K.S. Hariharan, S. Agarwal, S.B. Swernath, R. Bharti, S. Han, et al., Transfer learning based generalized framework for state of health estimation of Li-ion cells, Sci. Rep. 12 (2022) 13173, https://doi.org/10.1038/s41598-022-16692-4.
[45] Y. Li, K. Li, X. Liu, Y. Wang, L. Zhang, Lithium-ion battery capacity estimation — a pruned convolutional neural network approach assisted with transfer learning, Appl. Energy 285 (2021) 116410, https://doi.org/10.1016/j.apenergy.2020.116410.
[46] F. Yao, D. Meng, Y. Wu, Y. Wan, F. Ding, Online health estimation strategy with transfer learning for operating lithium-ion batteries, Journal of Power Electronics 23 (2023) 993–1003, https://doi.org/10.1007/s43236-023-00605-3.
[47] S. Tao, M. Zhang, Z. Zhao, H. Li, R. Ma, Y. Che, et al., Non-destructive degradation pattern decoupling for early battery trajectory prediction via physics-informed learning, Energy Environ. Sci. 18 (2025) 1544–1559, https://doi.org/10.1039/D4EE03839H.
[48] S. Tao, C. Sun, S. Fu, Y. Wang, R. Ma, Z. Han, et al., Battery cross-operation-condition lifetime prediction via interpretable feature engineering assisted adaptive machine learning, ACS Energy Lett. 8 (2023) 3269–3279, https://doi.org/10.1021/acsenergylett.3c01012.
[49] S. Tao, R. Guo, J. Lee, S. Moura, L.C. Casals, S. Jiang, et al., Immediate remaining capacity estimation of heterogeneous second-life lithium-ion batteries via deep generative transfer learning, Energy Environ. Sci. 18 (2025) 7413–7426, https://doi.org/10.1039/D5EE02217G.
[50] K. Zheng, J. Meng, Z. Yang, F. Zhou, K. Yang, Z. Song, Refined lithium-ion battery state of health estimation with charging segment adjustment, Appl. Energy 375 (2024) 124077, https://doi.org/10.1016/j.apenergy.2024.124077.
[51] S. Ji, Z. Zhang, H.S. Stein, J. Zhu, Flexible health prognosis of battery nonlinear aging using temporal transfer learning, Appl. Energy 377 (2025) 124766, https://doi.org/10.1016/j.apenergy.2024.124766.
[52] J. Lu, R. Xiong, J. Tian, C. Wang, F. Sun, Deep learning to estimate lithium-ion battery state of health without additional degradation experiments, Nat. Commun. 14 (2023) 2760, https://doi.org/10.1038/s41467-023-38458-w.
[53] B. Nowacki, T. Schmitt, P. Aquino, C. Hu, Fine-tuning for rapid capacity estimation of lithium-ion batteries, Energy Storage Mater. 81 (2025) 104425, https://doi.org/10.1016/j.ensm.2025.104425.
[54] J. Zhu, Y. Wang, Y. Huang, R. Bhushan Gopaluni, Y. Cao, M. Heere, et al., Data-driven capacity estimation of commercial lithium-ion batteries from voltage relaxation, Nat. Commun. 13 (2022) 2261, https://doi.org/10.1038/s41467-022-29837-w.
[55] L. Lu, P. Jin, G. Pang, Z. Zhang, G.E. Karniadakis, Learning nonlinear operators via DeepONet based on the universal approximation theorem of operators, Nat. Mach. Intell. 3 (2021) 218–229, https://doi.org/10.1038/s42256-021-00302-5.
[56] S.-Z. Chen, J. Liu, H. Yuan, Y. Tao, F. Xu, L. Yang, AM-MFF: a multi-feature fusion framework based on attention mechanism for robust and interpretable lithium-ion battery state of health estimation, Appl. Energy 381 (2025) 125116, https://doi.org/10.1016/j.apenergy.2024.125116.
[57] Z. Zhao, B. Liu, F. Wang, S. Zheng, Q. Yu, Z. Zhai, et al., Exploration of Imbalanced Regression in state-of-health estimation of lithium-ion batteries, J. Energy Storage 105 (2025) 114542, https://doi.org/10.1016/j.est.2024.114542.
[58] F. Wang, Z. Zhai, Z. Zhao, Y. Di, X. Chen, Physics-informed neural network for lithium-ion battery degradation stable modeling and prognosis, Nat. Commun. 15 (2024) 4332, https://doi.org/10.1038/s41467-024-48779-z.
[59] V. Krasteva, T. Stoyanov, I. Jekova, Implementing deep neural networks on ARM-Based microcontrollers: application for ventricular fibrillation detection, Appl. Sci. 15 (2025) 1965, https://doi.org/10.3390/app15041965.
[60] F. Berger, D. Joest, E. Barbers, K. Quade, Z. Wu, D.U. Sauer, et al., Benchmarking battery management system algorithms - requirements, scenarios and validation for automotive applications, eTransportation 22 (2024) 100355, https://doi.org/10.1016/j.etran.2024.100355.
[61] D.D. Tadoum, F. Berger, F. Krause, D. Wasylowski, F. Ringbeck, W. Li, et al., Standards and regulations for battery management systems in Germany: review and improvement potentials, Glob. Chall. 9 (2025) e00129, https://doi.org/10.1002/gch2.202500129.
[62] S.-Z. Chen, Z. Liang, H. Yuan, L. Yang, F. Xu, Y. Fan, A novel state of health estimation method for lithium-ion batteries based on constant-voltage charging partial data and convolutional neural network, Energy 283 (2023) 129103, https://doi.org/10.1016/j.energy.2023.129103.
[63] S. Zhang, H. Zhu, J. Wu, Z. Chen, Voltage relaxation-based state-of-health estimation of lithium-ion batteries using convolutional neural networks and transfer learning, J. Energy Storage 73 (2023) 108579, https://doi.org/10.1016/j.est.2023.108579.
[64] C. Liang, S. Tao, X. Huang, Y. Wang, B. Xia, X. Zhang, Stochastic state of health estimation for lithium-ion batteries with automated feature fusion using quantum convolutional neural network, J. Energy Chem. 106 (2025) 205–219, https://doi.org/10.1016/j.jechem.2025.02.030.
[65] C. Lin, L. Wu, X. Tuo, C. Liu, W. Zhang, Z. Huang, et al., A lightweight two-stage physics-informed neural network for SOH estimation of lithium-ion batteries with different chemistries, J. Energy Chem. 105 (2025) 261–279, https://doi.org/10.1016/j.jechem.2025.01.057.